3D polarization texture of a symmetric 4-fold flux closure domain in strained ferroelectric $PbTiO_3$ films

Y.L. Tang and Y.L. Zhu
Shenyang National Laboratory for Materials Science, Institute of Metal Research, Chinese Academy of Sciences, Shenyang 110016, China

Z.J. Hong
Department of Materials Science and Engineering, The Pennsylvania State University, University Park, Pennsylvania 16802, USA

E.A. Eliseev
Institute for Problems of Materials Science, National Academy of Sciences of Ukraine, Kyiv 03142, Ukraine

A.N. Morozovska
Institute of Physics, National Academy of Sciences of Ukraine, Kyiv 03028, Ukraine

Y.J. Wang, Y. Liu, Y.B. Xu, and B. Wu
Shenyang National Laboratory for Materials Science, Institute of Metal Research, Chinese Academy of Sciences, Shenyang 110016, China

L.Q. Chen
Department of Materials Science and Engineering, The Pennsylvania State University, University Park, Pennsylvania 16802, USA

S.J. Pennycook
Department of Materials Science and Engineering, National University of Singapore, Singapore 117576, Singapore

X.L. Ma[a)]
Shenyang National Laboratory for Materials Science, Institute of Metal Research, Chinese Academy of Sciences, Shenyang 110016, China

(Received 18 April 2016; accepted 23 June 2016)

Although the strong coupling of polarization to spontaneous strain in ferroelectrics would impart a flux-closure with severe disclination strains, recent studies have successfully stabilized such a domain via a nano-scaled multi-layer growth. Nonetheless, the detailed distributions of polarizations in three-dimensions (3D) and how the strains inside a flux closure affect the structures of domain walls are still less understood. Here we report a 3D polarization texture of a 4-fold flux closure domain identified in tensile strained ferroelectric $PbTiO_3/SrTiO_3$ multilayer films. Ferroelectric displacement analysis based on aberration-corrected scanning transmission electron microscopic imaging reveals highly inhomogeneous strains with strain gradient above 10^7/m. These giant disclination strains significantly broaden the 90° domain walls, while the flexoelectric coupling at 180° domain wall is less affected. The present observations are helpful for understanding the basics of topological dipole textures and indicate novel applications of ferroelectrics through engineering strains.

I. INTRODUCTION

Various spin textures such as skyrmions, helical orders, flux closures, or vortices have generated great interest recently not only for exploring previously ignored spin interaction mechanisms, but also for potential applications as high performance, low cost memories.[1–6] While ferromagnetic exchange favors parallel spin polarizations,[2] other mechanisms such as asymmetry interactions or demagnetization field tend to swing spins and thus form intriguing spin textures in magnets.[1–7] Nevertheless, a precondition for the occurrences of these novel spin structures is that the magnetic anisotropy energies are week forces so that spin can rotate continuously under specific conditions.[1,2,7]

Ferroelectric materials are the counterpart of ferromagnets. They are polar in structure which is switchable under an external field,[8] and therefore, are promising materials for random access memories, thin-film capacitors and actuators.[9,10] Nanoscale ferroelectrics were predicted to exhibit unique closure-quadrant patterns with closed head–tail dipole moments known as flux-closures.[11–15] These

Contributing Editor: Rafal Dunin-Borkowski
[a)]Address all correspondence to this author.
e-mail: xlma@imr.ac.cn
DOI: 10.1557/jmr.2016.259

flux-closure domains should be switchable which may give rise to an unusually high density of "bits" (Ref. 11) as well as potential applications in mechanical sensors and transducers.[14] Nevertheless, in ferroelectric materials, the coupling of polarization to spontaneous strain would be so remarkable that formation of a closure-quadrant with its resultant severe disclination strains is hard to reach.[7,16] Although closure-quadrants were reported in tetragonal ferroelectric $BaTiO_3$ (Refs. 17–19), $PbZr_{0.42}Ti_{0.58}O_3$ (Ref. 20) and PZN-12PT (Ref. 21), they are mostly composed of shape conserving 90° stripe domains or twins within each quadrant to accommodate the disclination strains. In such cases, the closure-quadrants may not always involve continuous dipole rotations. While continuous dipole rotations were observed in half of closure quadrants responding to depolarization fields,[22,23] another strategy, i.e., external strains were recently used to overcome the strongly coupled strains and polarizations in ferroelectrics and periodically arranged flux closure quadrants and polar vortices were obtained in tensile strained $PbTiO_3/SrTiO_3$ multilayers.[24,25] However, the fine distributions of polarizations in 3D and how the strains inside a flux closure affect the structures of domain walls are still less understood, especially little is known at the atomic level.

In this work, we show that external tensile strain from a $GdScO_3$ substrate could trigger symmetrical full flux closure featured as twin-free 4-fold domain wall junctions, in a $PbTiO_3/SrTiO_3$ (PTO/STO) multilayer film. On the basis of aberration-corrected high angle annular dark field (HAADF) Z-contrast scanning transmission electron microcopy (STEM), we have made precise determination of strains and relative ion displacement for individual PTO unit cells. Unusual disclination strains and 3D polarization texture as well as their effects on the domain walls inside the closure quadrant were observed and further rationalized by phase-field simulations and Landau–Ginsburg–Devonshire (LGD) phenomenological analytical calculations.

II. EXPERIMENTAL PROCEDURES

An epitaxial structure of $SrTiO_3$(10 nm)/$PbTiO_3$(38 nm)/$SrTiO_3$(3 nm)/$PbTiO_3$(26 nm) was grown on a $GdScO_3(110)_o$ substrate by pulsed laser deposition [PLD, Fig. 1(a), where the O subscripts represent orthorhombic indices here] using a Lambda Physik LPX 305i KrF (λ = 248 nm) excimer laser. The $PbTiO_3$ targets were 3 mol% Pb-enriched sintered ceramics. The target–substrate distance was 40 mm. The background pressure was 10^{-5} Pa. During the growth of PTO, the substrate temperature was kept at 650 °C, with a laser energy density of 2 J/cm^2, a laser repetition rate of 5 Hz and under an oxygen pressure of 20 Pa. For the growth of $SrTiO_3$ layers, the substrate temperature was also 650 °C, with a laser energy density of 1 J/cm^2, a laser repetition rate of 2 Hz and under an oxygen pressure of 8 Pa.[24] The $GdScO_3$ substrate has a larger pseudocubic lattice parameter (3.97 Å) than PTO (a = 3.90 Å), thus various 90° twins tend to form to relax the mismatch.[26] The strain coupling between 90° twins and the coherent PTO/STO interfaces may give rise to novel topological dipole textures as observed previously.[24] The high-quality PTO/STO multilayer can be identified in the low-magnification cross-sectional HAADF-STEM image and the corresponding well-defined intensity profile [Figs. 1(b) and 1(c)]. The final 10 nm STO layer was designed to negate any charge compensation of the surface which might affect the intrinsic domain patterns of the film.

The samples for the STEM experiments were prepared by slicing, gluing, grinding, dimpling, and finally ion milling. A Gatan PIPS was used for the final ion milling. HAADF images were recorded using aberration-corrected scanning transmission electron microscopes [Titan Cubed 60–300 kV microscope (FEI) fitted with a high-brightness field-emission gun (X-FEG) and double Cs corrector from CEOS operating at 300 kV]. The beam convergence angle is 25 mrad, and the collection angle ranges from 50 mrad to 250 mrad. Noise in the obtained HAADF-STEM images was reduced by Wiener filter or a low-pass annular mask restricted to the instrument resolution limit of the image. The atom positions were determined accurately by fitting them as two dimensional (2D) Gaussian peaks by using Matlab,[22–28] thus the lattice spacing and Ti^{4+} shifts (δ_{Ti}) were deduced (Fig. 2). The lattice parameters of PTO unit cells were determined though the Pb^{2+} column coordinates in the HAADF-STEM images. The atomic number for Pb^{2+} is high enough to produce extremely bright contrast, since the atomic column intensity in HAADF-STEM image is approximately proportional to Z^2 (Refs. 23–26). The coordinates of brighter Pb^{2+} columns were thus used to determine the lattice parameters, because of their high accuracy.[23] The lattice parameters were calibrated with reference to the lattice parameter of the $GdScO_3$ substrate in a low magnified HAADF-STEM image.

HAADF-STEM imaging is used to identify the structural details at the atomic scale. PTO has a tetragonal structure in which the positioning of cations and anions are schematically displayed in Fig. 2(a). Both the oxygen octahedra and the Ti cation have displacements from the center of Pb tetragonal cell that induce the spontaneous polarization [P_s, see the [100]-projection in Fig. 2(b)]. The displacement vectors of Ti^{4+} (denoted as δ_{Ti}) relative to the mass center of the four nearest Pb^{2+} neighbors [Fig. 2(c)] can be determined by fitting them as 2D Gaussian peaks based on the HAADF-STEM images.[22–28] The δ_{Ti} vector in each unit cell is opposite to the P_s direction of the PTO [Fig. 2(c)]. The δ_{Ti} vector

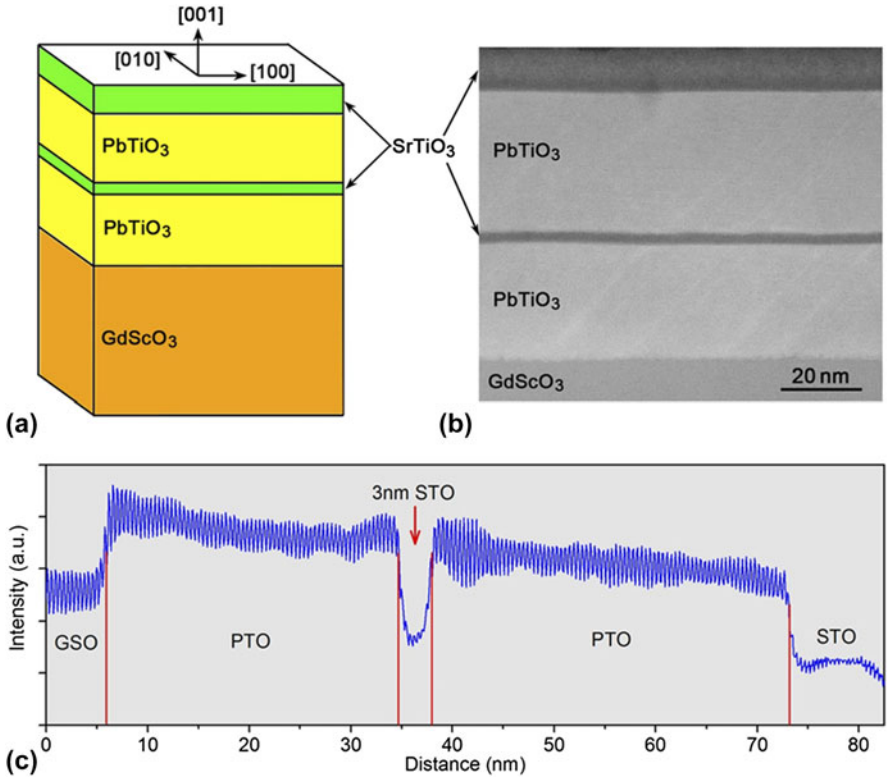

FIG. 1. Illustration of the heteroepitaxial $SrTiO_3$(10 nm)/$PbTiO_3$(36 nm)/$SrTiO_3$(3 nm)/$PbTiO_3$(28 nm)/$GdScO_3$ multilayer. (a) Schematic illustration of the multilayer. (b) A low-magnification cross-sectional HAADF-STEM image of the $PbTiO_3$/$SrTiO_3$ multilayer. (c) A HAADF-STEM intensity profile of (b), which reveals the well-grown $PbTiO_3$/$SrTiO_3$ multilayer. Since the image intensity under HAADF mode is about proportional to Z^2 (Z is the atomic number), heavy cations appear as bright contrast while light ions appear as gray contrast in the HAADF, or Z-contrast images. Thus in (b) $PbTiO_3$ crystal shows bright appearance, while the $SrTiO_3$ layers and $GdScO_3$ substrate exhibit darker contrast since Gd and Sr elements are much lighter than Pb.

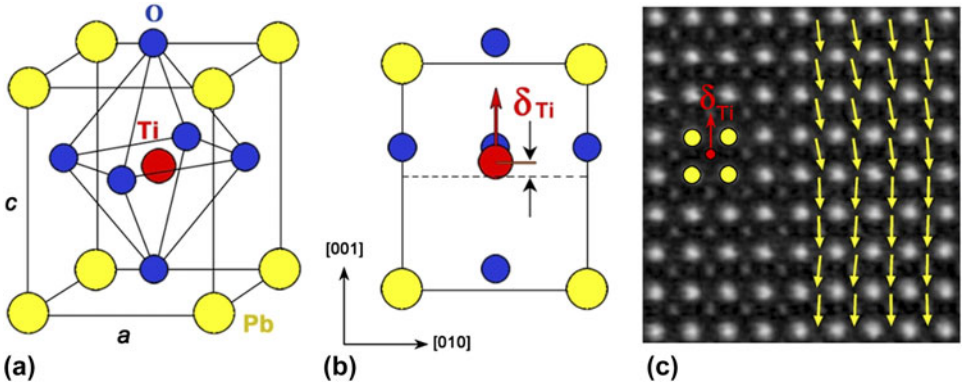

FIG. 2. Experimental determination of the polarization direction by the relative displacements of the Ti^{4+} cation columns and the Pb^{2+} cation columns. (a) Schematic perspective view of the unit cell of ferroelectric $PbTiO_3$. (b) Projection of the unit-cell along the [100] direction (yellow circle: Pb^{2+}, red circle: Ti^{4+} and blue circle: O^{2-}). (c) A HAADF-STEM image of the $PbTiO_3$ crystal. The image is recorded with the incident electron beam parallel to the [100] direction. The Pb^{2+} columns appear brighter than the Ti^{4+} columns. The red arrows in (b) and (c) denote the relative displacements of the Ti^{4+} columns and the Pb^{2+} columns, which were opposite to the spontaneous polarization direction of the $PbTiO_3$. Yellow arrows superimposed on the right panel of (c) indicate reversed Ti^{4+} ion displacement (δ_{Ti}) vectors, which were consistent with the spontaneous polarization direction of the $PbTiO_3$.

maps were smoothed using an averaging window of 1.2 nm. The visualization of the 2D δ_{Ti} vectors was carried out by using Matlab. The visualization of the lattice parameters and lattice rotations were carried out using the combination of Matlab and Gatan DigitalMicrograph software.

Phase-field simulation of domain structures of the PTO/STO multilayer film was stated from small slightly

polar nuclei and thus the stabilized domain structure of the multilayer under tensile strain was obtained. In this calculation, spontaneous polarization vectors are used as the order parameter, which is governed by the time dependent Ginzburg–Landau equations.[29–31] Moreover, the energy terms involving elastic and gradient components were also considered. The detailed solution to the phase-field equations can be found in literatures.[29,31] All the parameters can also be found in literature for PTO[29,32] and STO.[33] An iteration method is adopted to accommodate the elastic anisotropy between the PTO and STO layer.[34] A system size of 500 × 2 × 250 in three dimensions is used with each grid representing 0.4 nm, where 20 grids of substrate, 70 grids of PTO, 6 grids of STO, 90 grids of PTO, 25 grids of STO, and 39 grids of air in the thickness direction from the bottom is added to simulate the experimental condition. Short circuit electric boundary condition is assumed on the bottom and top of the film with compensation of charge from air. The mixed mechanical boundary condition is used where the film top is stress free and sufficient far away from the substrate bottom, the displacement is zero. Periodical boundary condition is used along the in-plane directions while a superposition method is applied on the out-of-plane dimension.[35]

III. RESULTS

Figure 3(a) is a low-magnification HAADF-STEM image of the PTO/STO multilayer showing the morphology of the whole film. The PTO layers can be easily distinguished here since they display brighter intensity in the Z-contrast image. Subtle contrast fluctuations can be identified in the PTO layers showing possible domain walls (DWs), which can be extracted by strain mapping via geometric phase analysis (GPA, Refs. 36 and 37), as shown in Fig. 3(b). Domains marked with red color have larger in-plane lattice parameter (*a* domain), while domains in green possess smaller in-plane lattice parameter (*c* domain). A periodic array of asymmetric flux closure quadrants is seen at the right side of the lower PTO layer.[24] A possible 4-fold domain wall junction displaying symmetric closure feature is marked with a yellow box. Since a symmetric flux closure quadrant is still elusive, here we focus on the atomic morphology and physical properties inside the symmetric flux closure.

The possible symmetric closure quadrant is magnified in Fig. 4. As can be seen, it is composed of two 3-fold DWs connected by a 180° DW [blue dashed-line, Fig. 4(a)]. An intersection of two 90° twins (green dashed-lines) can be identified at the lower panel of Fig. 4(a). A HAADF-STEM image superimposed with Ti^{4+} displacement maps unit-cell by unit-cell is shown in Fig. 4(b) (the unedited raw image of the symmetric closure quadrant is shown in Fig. 5). This is a quadrant head-to-tail polarization closure

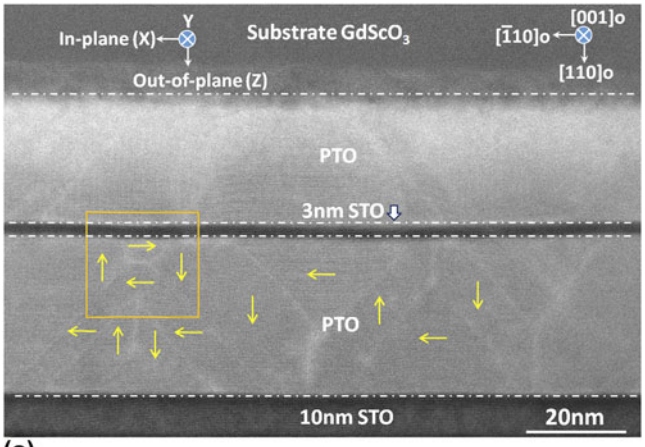

(a)

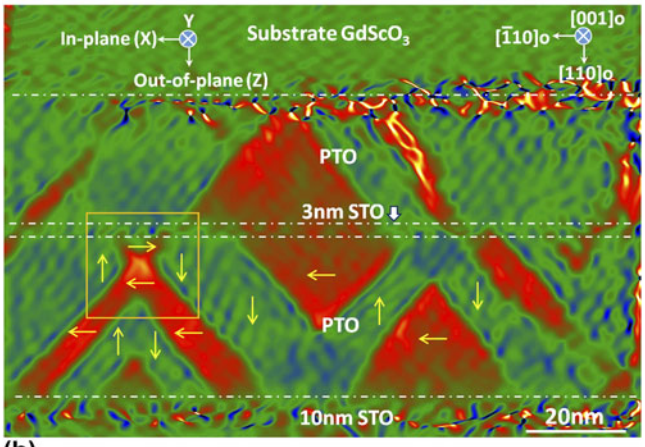

(b)

FIG. 3. HAADF-STEM image and in-plane strain analysis of the $PbTiO_3/SrTiO_3$ multilayer film. (a) A low-magnification HAADF-STEM image of the multilayer. (b) In-plane strain map extracted via GPA. Domains marked with red color have larger in-plane lattice parameter (*a* domain), while domains filled with green color possess smaller in-plane lattice parameter (*c* domain). Yellow arrows indicate possible polarization directions in corresponding domains, which will be specified in latter analysis (Figs. 4 and 5). Note that a possible 4-fold domain wall junctions displaying flux closure feature was marked by a yellow box.

domain composed of two 3-fold vertices. Such a configuration is just the one predicted by Charles Kittel as early as in 1946 for small ferromagnetic platelets[38] and proposed by Srolovitz and Scott in 1986 for ferroelectrics.[39] Strain maps [in-plane and out-of-plane lattice parameters, in-plane and out-of-plane lattice rotations shown in Figs. 6(a)–6(d), 'lattice rotation' here refers to rigid-body rotation of crystal lattice,[24,36,37] the detailed definitions were given in the inset of Fig. 6(d)] indicate a unique strain interaction mode of the two 90° twins and the STO layer [note the curvature of the 3 nm STO layer in Fig. 4(a)]. It is proposed that the coupling of 90° twins and the STO layer be responsible for such a special domain patterns. That is to say, these hourglass-like 90° twins form a completely closed (flux-closure) structure connected

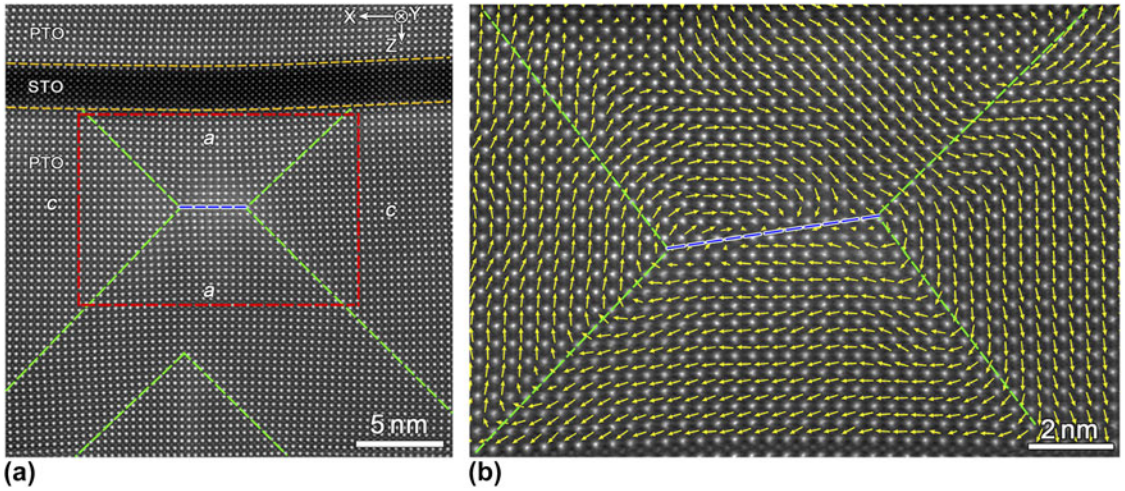

FIG. 4. HAADF-STEM imaging of the 4-fold domain wall junctions in the $PbTiO_3$ layer close to the 3 nm $SrTiO_3$ layer. (a) Atomic-resolution image of the $PbTiO_3/SrTiO_3$ multilayer. The Pb^{2+} ions appear as bright circles, the Sr^{2+} and Ti^{4+} ions show degressively changed intensities. The green dashed-lines trace the 90° domain walls. Note the curvature of the 3 nm $SrTiO_3$ layer, which implies that the upper and lower $PbTiO_3$ layers are strain-coupled with each other. The blue dotted-line indicates the 180° domain wall. (b) A magnification of the red box area in (a) superimposed with reversed Ti^{4+} ion displacement vector maps unit-cell by unit-cell. It is a quadrant head-to-tail polarization-closure domains composed of two 3-fold vertices.

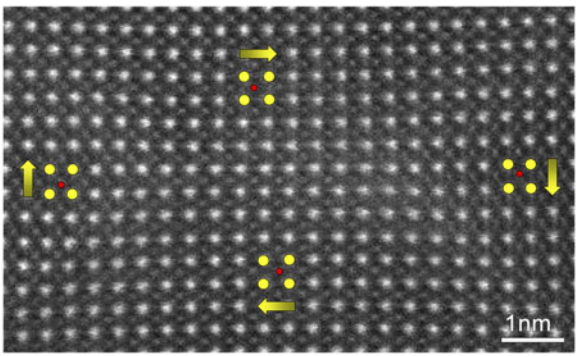

FIG. 5. High-magnification raw image of the 4-fold domain wall junctions corresponding to Fig. 4.

by four 90° DWs and one 180° DW, namely, a 4-fold domain wall junction. It is of great interest to notice that each quadrant is a single domain and free from any superfluous 90° twin to relax the disclination strains, so the strains in such a flux-closure are very unusual, as seen in the inhomogeneity of disclination strains shown in Figs. 6(a)–6(d). The in-plane strains beside the 180° DW accumulate a maximum around the two 3-fold vertices and decay gradually from the center to edges, while the in-plane strains at the left and right *c* domains are relatively homogeneous [Fig. 6(a)]. In contrast, the out-of-plane strains in each domain around the closure quadrant are relatively uniform [Fig. 6(c)]. The lattice rotation maps shown in Figs. 6(b) and 6(d) display remarkable disclination strain features, since the rotation of these perovskite lattices varies continuously from left to right even in a single domain.

To quantitatively reveal the lattice behaviors inside the 4-fold domain wall junctions, both the in-plane and out-of-plane lattice distributions as well as the tetragonality (*c*/*a*) across the 180° DW were statistically analyzed, as shown in Fig. 7. The data were acquired from the PTO unit cells corresponding to the white box area marked in Fig. 6(a). Distribution character of the in-plane lattice parameter (*c* lattice here) was consistent with the 2D strain map [Fig. 6(a)]. The lattice parameter gradient of this disclination strain can thus be estimated as 0.018 Å per unit cell and corresponds to a strain gradient above 10^7/m, which is, to the best of our knowledge, the highest one obtained in experiment (except for ferroelectric DWs and other interfaces, where large strain gradient up to 10^8–10^9/m may occur within a very local area, Ref. 24). In contrast, the out-of-plane lattice parameter (*a* lattice here) distributions shows an abnormal weak peak in the *a* domain near the 3 nm STO layer, which can also be inspected in the 2D strain map [Fig. 6(c)]. This abnormal elongation of the out-of-plane lattice is probably caused by a tensile strain from the above STO layer and the upper PTO layer, since the STO layer is obviously bended.

Such a combination of both the in-plane and out-of-plane lattice behaviors induces even more unusual *c*/*a* ratio distributions, as shown in Fig. 7(c). While the gradual reduction of tetragonality beside the 180° DW is reasonable and consistent with the in-plane lattice decreases, unusual *c*/*a* ratios smaller than 1 are observed for PTO unit cells near the 3 nm STO layer involving about 6 unit cells. Previous first-principles simulations indicated that this tetragonality behavior is the unique character of tetragonal ferroelectric vortex domains,[12] thus the results here provide direct observations of such novel strain states in topological dipole structures of ferroelectrics.

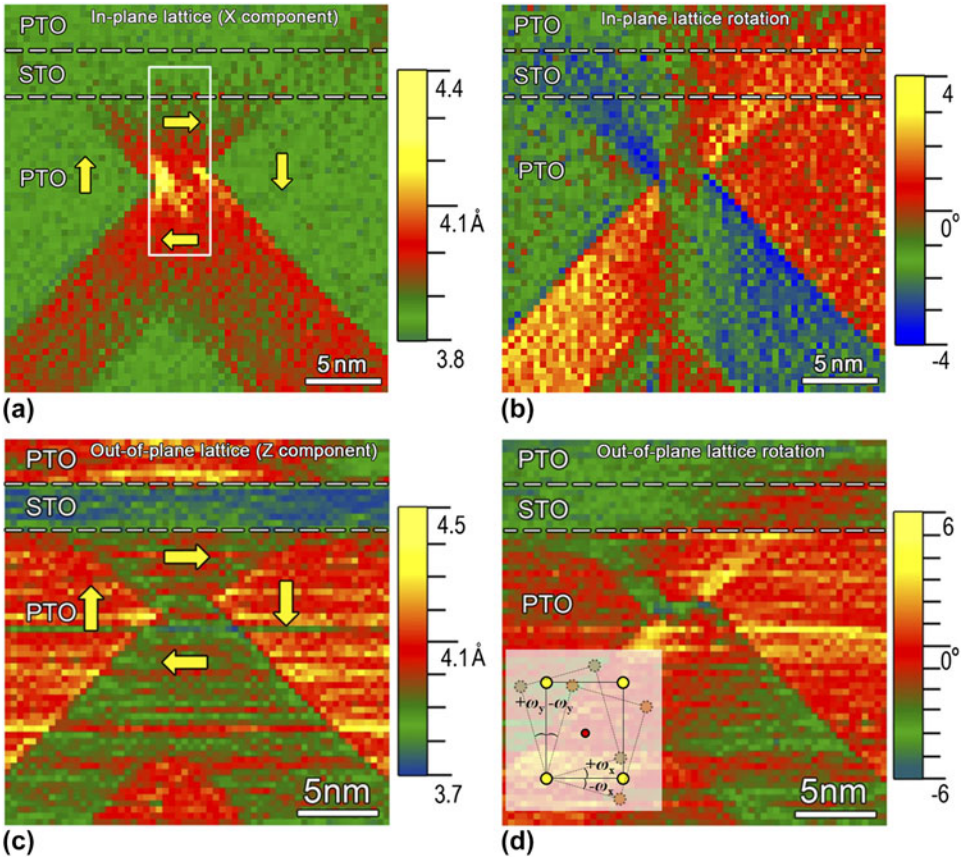

FIG. 6. Strain analysis of the 4-fold domain wall junctions in $PbTiO_3/SrTiO_3$ multilayer. (a and b) In-plane lattice parameters and in-plane lattice rotations mappings near the 4-fold domain wall junctions. (c and d) Out-of-plane lattice parameters and out-of-plane lattice rotations mappings near the 4-fold domain wall junctions. An inset in (d) indicates the definition of in-plane and out-of-plane lattice rotation. The in-plane lattice rotation was denoted by ω_x, while the out-of-plane lattice rotation was denoted by ω_y. Counter-clockwise lattice rotation was defined as positive rotation, while clockwise rotation was defined as negative ones.

The spontaneous polarizations of ferroelectrics are strongly coupled with strains since the dipole in each unit cell is driven by relative shifts of anions and cations, through chemical bonding.[8,10] Thus it is reasonable to conclude that the spontaneous polarization distributions inside the 4-fold domain wall junction should also exhibit unique features in response to the unusual strain characters. Taking into the account of the fact that the ferroelectric shifts of ions are generally tiny and difficult to be quantified, we further carry out phase-field simulations for extracting the domain structures and polarizations and rationalizing the unusual strains inside the 4-fold domain wall junctions. The phase-field methods have been showing great potential to understand the domain structures and physical properties of nanoscale ferroelectric films.[40–42]

First we successfully reproduce the domain structures of the tensile strained PTO/STO multilayer on the $GdScO_3$ substrate with specific layer thicknesses, as shown in Fig. 8. The initial structure was constructed according to the experimentally measured thicknesses of each layer [Fig. 8(a)]. Note that both of the 4-fold domain wall junction and the periodic array of asymmetric flux-closure quadrants were well reproduced through the phase-field calculations, which were consistent with the HAADF-STEM observations (Fig. 3). One interesting feature is that the *a*-domains can well penetrate through the thin STO layer, forming continuous long ferroelastic domains due to the long-range strain interaction between the up and bottom PTO layer, which is also observed experimentally [Fig. 3(b)]. At first glance of both the in-plane and out-of-plane polarization maps, inhomogeneous distributions of polarization in each single domain are obvious, since the strains in corresponding domains are also nonuniform.

The strains and polarization vectors inside the 4-fold domain wall junction marked with a yellow box in Figs. 8(b) and 8(c) were analyzed in detail, as shown in Fig. 9. The gradually changed in-plane lattice parameter and increased out-of-plane lattice parameter from the closure center were consistent with the experimental observations. Generally, larger in-plane parameter is shown in the *a* domain region, while larger out-of-plane domain can be found in the *c* domain region. However, anomaly

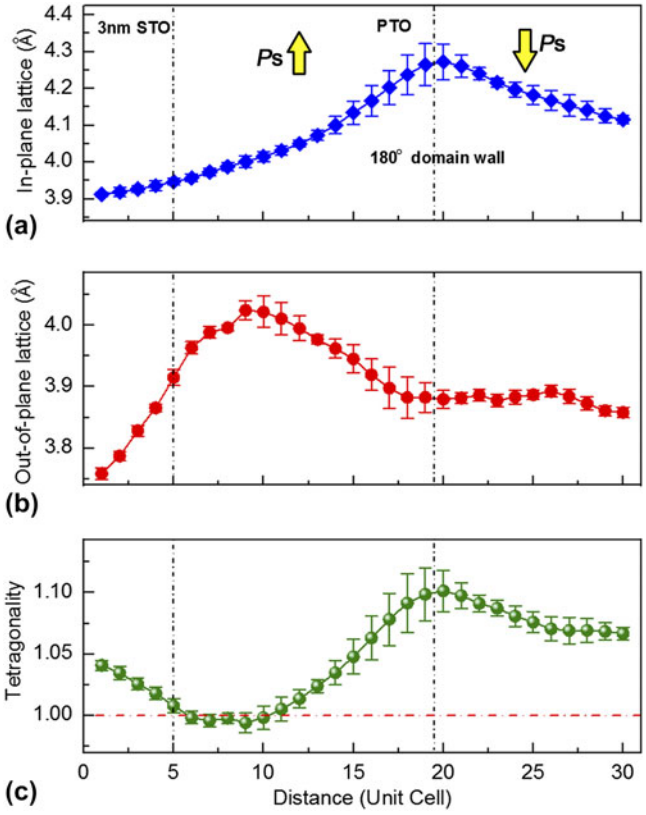

FIG. 7. Lattice behavior analysis across the 180° domain wall of the 4-fold domain wall junctions. (a) In-plane lattice parameter (*c* lattice here) distributions. The data was acquired from the white box area in Fig. 6(a). (b) Out-of-plane lattice parameter (*a* lattice here) distributions. The data was acquired from the $PbTiO_3$ unit-cells corresponding to the white box area marked in Fig. 6(a). (c) *c*/*a* ratio (tetragonality) distributions calculated based on (a) and (b). Note the giant lattice parameter gradient up to 0.018 Å per unit-cell in (a), corresponds to a strain gradient above 10^7/m. Also note an unusual a lattice peak in (b), which results in a nearly 1 tetragonality in (c). This unusual lattice behavior was predicted in first principle simulations for the ferroelectric vortices.[12]

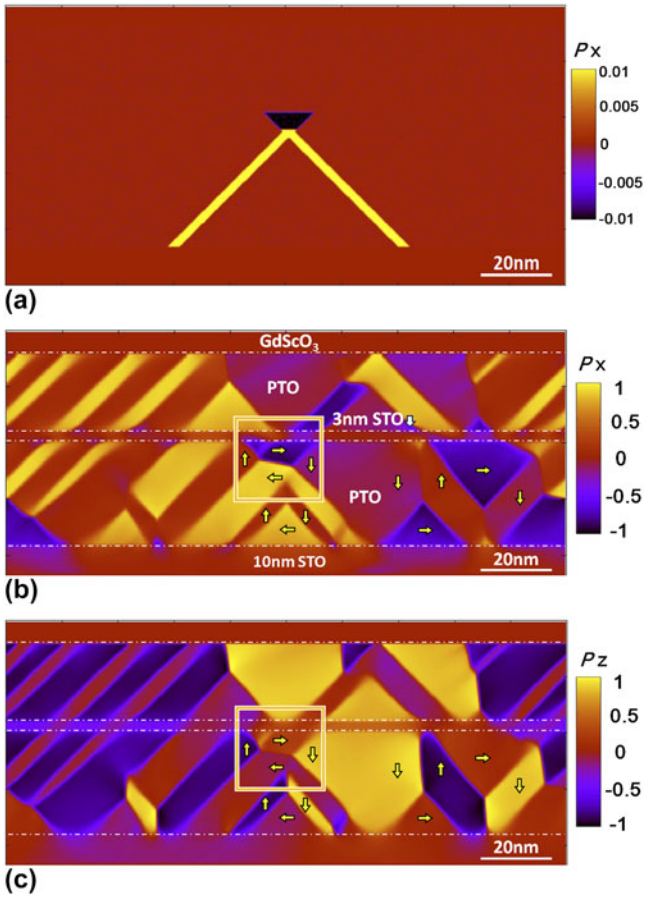

FIG. 8. Phase-field simulation of domain structures in the $PbTiO_3$/$SrTiO_3$ multilayer under tensile strain. (a) Initial structure used for the phase-field simulation of domain structures of the $PbTiO_3$/$SrTiO_3$ multilayer film. Small slightly polar nuclei were initiated until the stabilized domain structure obtained. (b) In-plane polarization map (*X* component). (c) Out-of-plane polarization map (*Z* component). Note that both of the 4-fold domain wall junctions and periodic array of flux-closure quadrants were well reproduced through the phase-field calculations, which are consistent with the HAADF-STEM observations (Fig. 3). The polarization of bulk $PbTiO_3$ (about 0.75 C/m^2) was normalized to '1' and used for defining the color scale of P_x and P_z.

develops near the PTO/STO interface, where both in-plane and out-of-plane lattice parameters tend to be in-between, close to 3.98 Å. The tetragonality of PTO unit cells near the STO/PTO interface equals about 1, since for these unit cells both of the in-plane and out-of-plane lattice constants have similar values. *X*–*Z* component polarization vector maps for the white box area marked in Fig. 9(b) display the 90 and 180° DWs directly [Fig. 9(c)]. There is an obvious reduction of polarizations beside the 180° DW. Note that evident polarization rotations away from the *c* axis occur above the 180° DW. Moreover, both the strain and polarization vector maps indicate that the two 90° DWs above the 180° DW are significantly broadened as compared with the other two 90° DWs. Particularly, dipoles across the upper two 90° DWs gradually and continuously rotate, which is in accordance with the DW broadening effects. More importantly, abnormal polarization component normal to the print page was further identified, as shown in Fig. 9(d), making locally lower symmetry phases. This lower symmetry phase can well explain the tetragonality near the PTO/STO interface. The strongly coupled lattice and polarization have induced complex 3D polarization distributions in response to the symmetry breaking of the lattice here inside the 4-fold domain wall junction.

Moreover, Landau–Ginsburg–Devonshire (LGD) phenomenology indicates that the flexoelectric coupling at the 180° DW of tetragonal ferroelectrics causes obvious lattice offsets in domains beside the 180° DW and lowers the symmetry of such a DW.[24,43–45] The offsets between 180° domains in PTO were also predicted in previous first principles calulations.[46] To reveal the flexoelectric

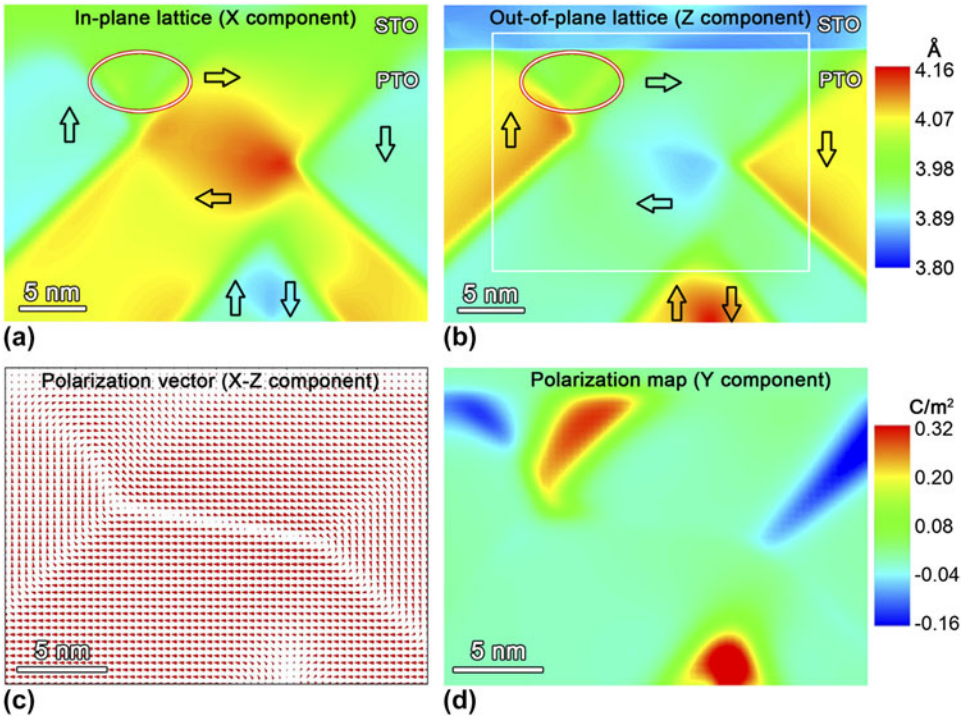

FIG. 9. Phase-field simulations of strain and polarization distributions in the 4-fold domain wall junctions. (a) In-plane lattice parameter map (X component). (b) Out-of-plane lattice parameter map (Z component). (c) Polarization vector map for the X–Z component. (d) Y component polarization map. Maps (c) and (d) correspond to the white box area marked in (b). Note that the color scales for the X and Z strain components in the ellipse areas are nearly the same, indicating a ~ 1 c/a ratio occurs here, which are consistent with the STEM observations [Fig. 7(c)].

coupling here at the 180° DW, the statistical distributions of Pb^{2+} offsets across the 180° DW in the 4-fold domain wall junction are shown in Figs. 10(a) and 10(b). A 180° DW in PTO single layer film grown on $SrTiO_3(001)$ was used as a reference, as shown in Figs. 10(c) and 10(d). The PTO crystal here is less affected by strain, since the mismatch between PTO (a = 3.90 Å) and $SrTiO_3(001)$ (a = 3.905 Å) substrate is tiny (<0.13%). Thus Fig. 10(d) reveals the intrinsic Pb^{2+} offsets across a 180° DW in tetragonal PTO crystal, which is about 0.72 Å. This value is in agreement with previous theoretical simulations, where an offset of 0.6 Å was reported for PTO.[46] Note the obvious scattering of Pb^{2+} offset distributions across the 180° DW in the 4-fold domain wall junction [Fig. 10(b)]. Nevertheless, the fitting results revealed that the relative Pb^{2+} offsets across these two 180° DWs were basically the same [Figs. 10(b) and 10(d)], while the Pb^{2+} offsets for 4-fold domain wall junction are highly asymmetric, especially for the left domain of Fig. 10(a), which is the a domain near the 3 nm STO layer exhibiting large strain gradient and nearly 1 tetragonality (Figs. 6 and 7). Thus we can conclude that the flexoelectric contribution on the structure of the 180° DW in the 4-fold domain wall junction is still less affected by the abnormal long range strain effects here. According to the LGD phenomenology,[47–49] the displacement component U_3 along the 180 DW can be deduced as:

$$U_3 = Q_{11}P_s^2 x_3 - F_{44}P_3(x_1) \quad ,$$

where Q_{11} is an electrostriction coefficient, P_s is the spontaneous polarization, x_3 is the coordinate along the 180° DW, and F_{44} is a flexoelectric effect tensor coefficient. The first term of U_3 originate from the electrostriction effect and represents constant spontaneous strain which is the same for both domains, while the second one origins from the flexoelectric effect displaying different signs for different 180° domains. Hence the difference (offset) between domains is[43]:

$$\delta U_3 = 2F_{44}P_s \quad .$$

Using P_s = 0.75 C/m^2 and the experimentally observed $\delta U_3 \approx 0.7$ Å, the flexoelectric coefficient F_{44} can thus be estimated as about 0.5 × 10^{-10} C^{-1} m^3, for both of the 180° DW in the 4-fold domain wall junction [Fig. 10(b)] and that in the strainless PTO film [Fig. 10(d)].

IV. DISCUSSIONS

Dipole rotation was thought to be not tolerated in these flux-closure structures at all length scales, even in ferroelectric compositions close to the Morphotropic Phase Boundary.[21] However, our results provide direct

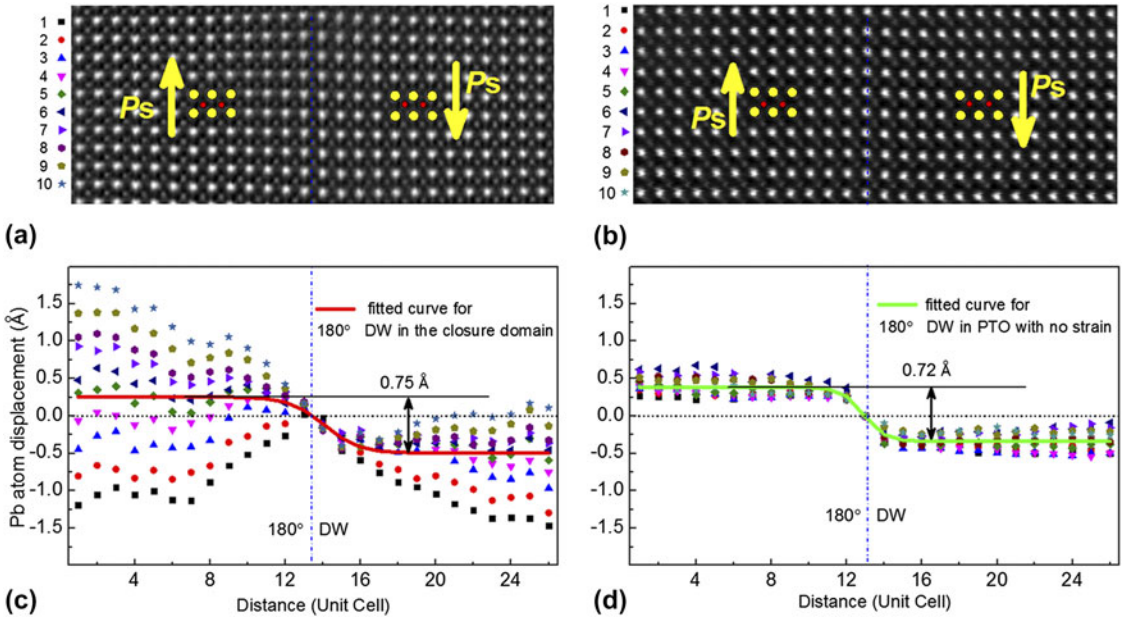

FIG. 10. Comparisons of Pb^{2+} ion offsets across the 180° domain wall in the 4-fold domain wall junctions and a 180° domain wall under no strain. These Pb^{2+} offsets were analyzed by the Landau–Ginsburg–Devonshire model. (a) The HAADF-STEM image of the 180° domain wall in the 4-fold domain wall junctions. (b) The distributions of Pb^{2+} offsets across the 180° domain wall in (a). The solid curve is the fitting result of the HAADF-STEM experiment based on (a). (c) A HAADF-STEM image of a 180° domain wall in a $PbTiO_3/SrTiO_3(001)$ film. The $PbTiO_3$ crystal here is less affected by strain since the mismatch between $PbTiO_3$ and $SrTiO_3(001)$ substrate is tiny (<0.13%). (d) The distributions of Pb^{2+} offsets across the 180° domain wall in (c). The solid curve is the fitting result based on the HAADF-STEM experiment of (c). Note the obvious scattering of Pb^{2+} offset distributions across the 180° domain wall in the 4-fold domain wall junctions in (c). Nevertheless, the fitting results revealed that the relative Pb^{2+} offsets across these two 180° domain walls were basically the same, while the Pb^{2+} offsets for 4-fold domain wall junctions are highly asymmetric.

experimental evidence of the continuous rotation of electrical dipoles forming full closure quadrants in a ferroelectric with strong tetragonality. The dimension of the 4-fold domain wall junction is found to be limited within about 20 nm (Fig. 3). This may indicate that the twin free closure quadrant occurs within narrow areas and large scale full closure should be energetically unfavorable as theoretically prodicted.[13] In contrast, the periodic arranged asymmetric closure arrays observed in a series of tensile strained PTO/STO multilayer films could extend over a large scale through unique strain compensation of disclination dipoles.[24]

Our results indicate that external strains from the substrates are essential for surpassing the electrostriction (of 10^{-2} orders, and the spontaneous strain is large as about 6.5% for PTO) and giving rise to the full flux closure states in ferroelectrics. In this aspect, it is an opposite of the counterpart in ferromagnets, where the magnetostriction is of 10^{-5} orders, thus the vortex spin states are spontaneously formed to lower magnetostatic energy with negligible elastic energy cost.[7,16,50] Particularly, recent experiments also confirmed that the external strains could also facilitate the depolarization field driven ferroelectric vortex states in strain engineered PTO/STO superlattice.[25] In other words, the observed closure structures here and in our previous study are possible precursors of condensations of electrical dipoles as ferroelectric vortices.[24,25]

At an application viewpoint, dipole closures in both of ferromagnetics and ferroelectrics sound promising.[1,5,9,11] Recent studies on ferromagnetic Fe-based alloys have found non-volume-conserving and hysteresis-free magnetostriction effects caused by reorientation of large scale 4-fold domain wall junction structures,[51] which indicate new magnetostrictive materials with high performance. We thus expect future explorations on large-scaling of the 4-fold domain wall junction structures in ferroelectric materials via engineering strains and consequently figuring out their field-dependent responses. We see that preliminary studies on dynamic characters of twin-relaxed ferroelectric closure domains are ongoing recently.[52] Thus novel units based on controllable flux closure domains in ferroelectrics are expected to be fabricated for investigating the dynamical responses and in turn helpful in the development of potential nanoscale ferroelectric devices.

V. CONCLUSIONS

We report a 3D polarization texture in a flux-closure quadrant identified in tensile strained ferroelectric $PbTiO_3/SrTiO_3$ multilayer films. Ferroelectric

displacement analysis based on aberration-corrected scanning transmission electron microscopic imaging reveals highly inhomogeneous strains and polarizations as responses to symmetry breaking. The lattice parameter gradient of this disclination strain is estimated as 0.018 Å per unit cell and corresponds to a strain gradient above 10^7/m. The 90° domain walls in the quadrant were significantly broadened with continuous dipole rotations and a complex 3D polarization texture was envisioned via phase-field modeling. The Landau–Ginsburg–Devonshire phenomenology reveals a lattice offset between 180° domains through flexoelectric coupling, which was less affected by the disclination strains inside the closure quadrant. Present observations are helpful for understanding the basics of topological dipole textures and indicate novel applications of ferroelectrics through strain engineering.

ACKNOWLEDGMENTS

This work is supported by the National Natural Science Foundation of China (No. 51231007, 51571197, 51501194 and 51521091) and National Basic Research Program of China (2014CB921002). Y.L.T. acknowledges the IMR SYNL-T.S. Kê Research Fellowship and the Youth Innovation Promotion Association CAS (No. 2016177). A.N.M. and E.A.E. acknowledge the financial support from the National Academy of Science of the Ukraine. Z.J.H. gratefully acknowledges the US National Science Foundation under NSF DMR-1210588 and DMR-1420620, and L-Q.C. acknowledges the U.S. Department of Energy, Office of Basic Energy Sciences, Division of Materials Sciences and Engineering under Award DE-FG02-07ER46417.

REFERENCES

1. T. Shinjo, T. Okuno, R. Hassdorf, K. Shigeto, and T. Ono: Magnetic vortex core observation in circular dots of permalloy. *Science* **289**, 930 (2000).
2. U.K. Rößler, A.N. Bogdanov, and C. Pfleiderer: Spontaneous skyrmion ground states in magnetic metals. *Nature* **442**, 797 (2006).
3. M. Uchida, Y. Onose, Y. Matsui, and Y. Tokura: Real-space observation of helical spin order. *Science* **311**, 359 (2006).
4. X.Z. Yu, Y. Onose, N. Kanazawa, J.H. Park, J.H. Han, Y. Matsui, N. Nagaosa, and Y. Tokura: Real-space observation of a two-dimensional skyrmion crystal. *Nature* **465**, 901 (2010).
5. N. Romming, C. Hanneken, M. Menzel, J.E. Bickel, B. Wolter, K. von Bergmann, A. Kubetzka, and R. Wiesendanger: Writing and deleting single magnetic skyrmions. *Science* **341**, 636 (2013).
6. N. Nagaosa and Y. Tokura: Topological properties and dynamics of magnetic skyrmions. *Nature Nanotech.* **8**, 899 (2013).
7. G. Catalan, J. Seidel, R. Ramesh, and J.F. Scott: Domain wall nanoelectronics. *Rev. Mod. Phys.* **84**, 119 (2012).
8. R.E. Cohen: Origin of ferroelectricity in perovskite oxides. *Nature* **358**, 136 (1992).
9. J.F. Scott: Applications of modern ferroelectrics. *Science* **315**, 954 (2007).
10. N.A. Spaldin: Analogies and differences between ferroelectrics and ferromagnets. In *Physics of Ferroelectrics a Modern Perspective*. Topics in Applied Physics, Vol. **105**, K.M. Rabe, C.H. Ahn and J-M. Triscone eds.; Springer-Verlag, Berlin Heidelberg, 2007; pp. 175–218.
11. I.I. Naumov, L. Bellaiche, and H. Fu: Unusual phase transitions in ferroelectric nanodisks and nanorods. *Nature* **432**, 737 (2004).
12. S. Prosandeev and L. Bellaiche: Characteristics and signatures of dipole vortices in ferroelectric nanodots: First-principles-based simulations and analytical expressions. *Phys. Rev. B: Condens. Matter Mater. Phys.* **75**, 094102 (2007).
13. P. Aguado-Puente and J. Junquera: Ferromagnetic like closure domains in ferroelectric ultrathin films: First-principles simulations. *Phys. Rev. Lett.* **100**, 177601 (2008).
14. W.J. Chen, Y. Zheng, and B. Wang: Vortex domain structure in ferroelectric nanoplatelets and control of its transformation by mechanical load. *Sci. Rep.* **2**(796), 00796 (2012).
15. Z.D. Zhou and D.Y. Wu: Domain structures of ferroelectric films under different electrical boundary conditions. *AIP Adv.* **5**, 107206 (2015).
16. C. Kittel: Physical theory of ferromagnetic domains. *Rev. Mod. Phys.* **21**, 541 (1949).
17. A. Schilling, D. Byrne, G. Catalan, K.G. Webber, Y.A. Genenko, G.S. Wu, J.F. Scott, and J.M. Gregg: Domains in ferroelectric nanodots. *Nano Lett.* **9**, 3359 (2009).
18. L.J. McGilly, A. Schilling, and J.M. Gregg: Domain bundle boundaries in single crystal $BaTiO_3$ lamellae: Searching for naturally forming dipole flux-closure/quadrupole chains. *Nano Lett.* **10**, 4200 (2010).
19. R.G.P. McQuaid, L.J. McGilly, P. Sharma, A. Gruverman, and J.M. Gregg: Mesoscale flux-closure domain formation in single-crystal $BaTiO_3$. *Nat. Commun.* **2**(404), 1413 (2011).
20. L.J. McGilly and J.M. Gregg: Polarization closure in $PbZr_{(0.42)}Ti_{(0.58)}O_3$ nanodots. *Nano Lett.* **11**, 4490 (2011).
21. L-W. Chang, V. Nagarajan, J.F. Scott, and J.M. Gregg: Self-similar nested flux closure structures in a tetragonal ferroelectric. *Nano Lett.* **13**, 2553 (2013).
22. C.L. Jia, K.W. Urban, M. Alexe, D. Hesse, and I. Vrejoiu: Direct observation of continuous electric dipole rotation in flux-closure domains in ferroelectric $Pb(Zr,Ti)O_3$. *Science* **331**, 1420 (2011).
23. C.T. Nelson, B. Winchester, Y. Zhang, S-J. Kim, A. Melville, C. Adamo, C.M. Folkman, S-H. Baek, C-B. Eom, D.G. Schlom, L-Q. Chen, and X. Pan: Spontaneous vortex nanodomain arrays at ferroelectric heterointerfaces. *Nano Lett.* **11**, 828 (2011).
24. Y.L. Tang, Y.L. Zhu, X.L. Ma, A.Y. Borisevich, A.N. Morozovska, E.A. Eliseev, W.Y. Wang, Y.J. Wang, Y.B. Xu, Z.D. Zhang, and S.J. Pennycook: Observation of a periodic array of flux-closure quadrants in strained ferroelectric $PbTiO_3$ films. *Science* **348**, 547 (2015).
25. A.K. Yadav, C.T. Nelson, S.L. Hsu, Z. Hong, J.D. Clarkson, C.M. Schlepütz, A.R. Damodaran, P. Shafer, E. Arenholz, L.R. Dedon, D. Chen, A. Vishwanath, A.M. Minor, L.Q. Chen, J.F. Scott, L.W. Martin, and R. Ramesh: Observation of polar vortices in oxide superlattices. *Nature* **530**, 198 (2016).
26. G. Catalan, A. Lubk, A.H.G. Vlooswijk, E. Snoeck, C. Magen, A. Janssens, G. Rispens, G. Rijnders, D.H.A. Blank, and B. Noheda: Flexoelectric rotation of polarization in ferroelectric thin films. *Nat. Mater.* **10**, 963–967 (2011).
27. S.M. Anthony and S. Granick: Image analysis with rapid and accurate two-dimensional Gaussian fitting. *Langmuir* **25**, 8152–8160 (2009).
28. C-L. Jia, V. Nagarajan, J-Q. He, L. Houben, T. Zhao, R. Ramesh, K. Urban, and R. Waser: Unit-cell scale mapping of ferroelectricity and tetragonality in epitaxial ultrathin ferroelectric films. *Nat. Mater.* **6**, 64 (2007).

29. Y.L. Li, S.Y. Hu, Z.K. Liu, and L.Q. Chen: Effect of substrate constraint on the stability and evolution of ferroelectric domain structures in thin films. *Acta Mater.* **50**, 395 (2002).
30. L.Q. Chen: Phase-field method of phase transitions/domain structures in ferroelectric thin films: A review. *J. Am. Ceram. Soc.* **91**, 1835–1844 (2008).
31. Y.L. Li, S.Y. Hu, Z.K. Liu, and L.Q. Chen: Effect of electrical boundary conditions on ferroelectric domain structures in thin films. *Appl. Phys. Lett.* **81**, 427–429 (2002).
32. M.J. Haun: Ph.D Thesis, The Pennsylvania State University, 1988.
33. G. Sheng, Y.L. Li, J.X. Zhang, S. Choudhury, Q.X. Jia, V. Gopalan, D.G. Schlom, Z.K. Liu, and L.Q. Chen: A modified Landau–Devonshire thermodynamic potential for strontium titanate. *Appl. Phys. Lett.* **96**, 232902 (2010).
34. J.J. Wang, X.Q. Ma, Q. Li, J. Britson, and L.Q. Chen: Phase transitions and domain structures of ferroelectric nanoparticles: Phase field model incorporating strong elastic and dielectric inhomogeneity. *Acta Mater.* **61**, 7591–7603 (2013).
35. L.Q. Chen and J. Shen: Applications of semi-implicit Fourier-spectral method to phase field equations. *Comput. Phys. Commun.* **108**, 147–158 (1998).
36. M.J. Hÿtch, E. Snoeck, and R. Kilaas: Quantitative measurement of displacement and strain fields from HREM micrographs. *Ultramicroscopy* **74**, 131–146 (1998).
37. Y.L. Tang, Y.L. Zhu, and X.L. Ma: On the benefit of aberration-corrected HAADF-STEM for strain determination and its application to tailoring ferroelectric domain patterns. *Ultramicroscopy* **160**, 57–63 (2016).
38. C. Kittel: Theory of the structure of ferromagnetic domains in films and small particles. *Phys. Rev.* **70**, 965 (1946).
39. D.J. Srolovitz and J.F. Scott: Clock-model description of incommensurate ferroelectric films and of nematic-liquid-crystal films. *Phys. Rev. B: Condens. Matter Mater. Phys.* **34**, 1815 (1986).
40. N. Balke, S. Choudhury, S. Jesse, M. Huijben, Y.H. Chu, A.P. Baddorf, L.Q. Chen, R. Ramesh, and S.V. Kalinin: Deterministic control of ferroelastic switching in multiferroic materials. *Nat. Nanotechnol.* **4**, 868–875 (2009).
41. J. Slutsker, A. Artemev, and A. Roytburd: Phase-field modeling of domain structure of confined nanoferroelectrics. *Phys. Rev. Lett.* **100**, 087602 (2008).
42. D. Lee, H. Lu, Y. Gu, S-Y. Choi, S-D. Li, S. Ryu, T.R. Paudel, K. Song, E. Mikheev, S. Lee, S. Stemmer, D.A. Tenne, S.H. Oh, E.Y. Tsymbal, X. Wu, L-Q. Chen, A. Gruverman, and C.B. Eom: Emergence of room-temperature ferroelectricity at reduced dimensions. *Science* **349**, 1314 (2015).
43. A.K. Tagantsev, L.E. Cross, and J. Fousek: Chapter 6. In *Domains in Ferroic Crystals and Thin Films*. (Springer, New York, 2010); pp. 300–304.
44. P.V. Yudin, A.K. Tagantsev, E.A. Eliseev, A.N. Morozovska, and N. Setter: Bichiral structure of ferroelectric domain walls driven by flexoelectricity. *Phys. Rev. B: Condens. Matter Mater. Phys.* **86**, 134102 (2012).
45. E.A. Eliseev, P.V. Yudin, S.V. Kalinin, N. Setter, A.K. Tagantsev, and A.N. Morozovska: Structural phase transitions and electronic phenomena at 180-degree domain walls in rhombohedral $BaTiO_3$. *Phys. Rev. B: Condens. Matter Mater. Phys.* **87**, 054111 (2013).
46. B. Meyer and D. Vanderbilt: Ab initio study of ferroelectric domain walls in $PbTiO_3$. *Phys. Rev. B: Condens. Matter Mater. Phys.* **65**, 104111 (2002).
47. J.F. Nye: *Physical Properties of Crystals: Their Representation by Tensors and Matrices* (Clarendon Press, Oxford, 1985).
48. A.L. Roitburd: Equilibrium structure of epitaxial layers. *Phys. Status Solidi A* **37**, 329 (1976).
49. A.K. Tagantsev, G. Gerra, and N. Setter: Short-range and long-range contributions to the size effect in metal-ferroelectric-metal heterostructures. *Phys. Rev. B: Condens. Matter Mater. Phys.* **77**, 174111 (2008).
50. P. Chandra and P.B. Littelwood: A landau primer for ferroelectrics. In *Physics of Ferroelectrics a Modern Perspective*, Topics Applied Physics, Vol. **105**, K.M. Rabe, C.H. Ahn and J-M. Triscone eds.; Springer-Verlag, Berlin Heidelberg, 2007; pp. 69–116.
51. H.D. Chopra and M. Wuttig: Non-Joulian magnetostriction. *Nature* **521**, 340 (2015).
52. R.G. McQuaid, A. Gruverman, J.F. Scott, and J.M. Gregg: Exploring vertex interactions in ferroelectric flux-closure domains. *Nano Lett.* **14**, 4230–4237 (2014).